Journal of Advanced Ceramics
2022, **11**(8): 1279–1293
https://doi.org/10.1007/s40145-022-0609-z
ISSN 2226-4108
CN 10-1154/TQ

Research Article

$(Ho_{0.25}Lu_{0.25}Yb_{0.25}Eu_{0.25})_2SiO_5$ high-entropy ceramic with low thermal conductivity, tunable thermal expansion coefficient, and excellent resistance to CMAS corrosion

Zhilin CHEN[a], Zhilin TIAN[a,*], Liya ZHENG[a], Keyu MING[a], Xiaomin REN[b,c], Jingyang WANG[b], Bin LI[a,*]

[a]*School of Materials, Shenzhen Campus of Sun Yat-sen University, Shenzhen 518107, China*
[b]*Shenyang National Laboratory for Materials Science, Institute of Metal Research, Chinese Academy of Sciences, Shenyang 110016, China*
[c]*School of Materials Science and Engineering, University of Science and Technology of China, Hefei 230026, China*

Received: December 5, 2021; Revised: April 18, 2022; Accepted: May 1, 2022

Abstract: Low thermal conductivity, compatible thermal expansion coefficient, and good calcium–magnesium–aluminosilicate (CMAS) corrosion resistance are critical requirements of environmental barrier coatings for silicon-based ceramics. Rare earth silicates have been recognized as one of the most promising environmental barrier coating candidates for good water vapor corrosion resistance. However, the relatively high thermal conductivity and high thermal expansion coefficient limit the practical application. Inspired by the high entropy effect, a novel rare earth monosilicate solid solution $(Ho_{0.25}Lu_{0.25}Yb_{0.25}Eu_{0.25})_2SiO_5$ was designed to improve the overall performance. The as-synthesized $(Ho_{0.25}Lu_{0.25}Yb_{0.25}Eu_{0.25})_2SiO_5$ shows very low thermal conductivity (1.07 $W \cdot m^{-1} \cdot K^{-1}$ at 600 ℃). Point defects including mass mismatch and oxygen vacancies mainly contribute to the good thermal insulation properties. The thermal expansion coefficient of $(Ho_{0.25}Lu_{0.25}Yb_{0.25}Eu_{0.25})_2SiO_5$ can be decreased to $(4.0–5.9)\times10^{-6}$ K^{-1} due to severe lattice distortion and chemical bonding variation, which matches well with that of SiC ($(4.5–5.5)\times10^{-6}$ K^{-1}). In addition, $(Ho_{0.25}Lu_{0.25}Yb_{0.25}Eu_{0.25})_2SiO_5$ presents good resistance to CMAS corrosion. The improved performance of $(Ho_{0.25}Lu_{0.25}Yb_{0.25}Eu_{0.25})_2SiO_5$ highlights it as a promising environmental barrier coating candidate.

Keywords: high-entropy ceramic; environmental barrier coating (EBC); rare earth silicate; thermal conductivity; thermal expansion coefficient (TEC)

1 Introduction

The requirement for higher efficiency and better performance of gas turbine engines has led to unprecedented temperatures in the gas inlet. Even with the gas film cooling technology and protection of thermal barrier coatings (TBCs), superalloys can hardly meet the high-temperature demand [1]. SiC_f/SiC ceramic matrix composites (CMCs) with good high-temperature capability and excellent mechanical properties are

* Corresponding authors.
E-mail: Z. Tian, tianzhlin@mail.sysu.edu.cn;
B. Li, libin75@mail.sysu.edu.cn

promising candidates for replacing superalloys as hot-section components [2]. Unfortunately, SiC_f/SiC CMCs are susceptible to damage by oxygen and steam in harsh environments [3,4]. Thus, environmental barrier coatings (EBCs) are required to protect SiC_f/SiC CMCs by blocking the entry of oxygen and steam [5,6].

In addition to excellent resistance to the ingression of oxygen and steam, EBC should also be resistant to the attack of molten calcium–magnesium–aluminosilicate (CMAS). Based on that, the low thermal conductivity and compatible thermal expansion coefficient (TEC) are needed to enhance the thermal insulation properties and release the thermal stress during the thermal cycling process [6–8]. So far, EBC has been developed for three generations [9,10], and rare earth (RE) silicates, such as RE_2SiO_5 and $RE_2Si_2O_7$, are the most promising EBC candidates [11–14]. However, it is difficult to find a RE silicate ceramic with optimal thermal, mechanical, and corrosion-resistant properties. For example, Lu_2SiO_5 possesses the best resistance to CMAS corrosion at 1300 ℃, but relatively high thermal conductivity [12,15]. Ho_2SiO_5 has excellent bending strength and low thermal conductivity, but relatively low CMAS corrosion resistance [12,15]. Therefore, there is an urgent need to improve the properties of RE silicates for extreme environmental applications. Recently, high-entropy ceramics have been widely investigated, including oxides, borides, and carbides, which have been shown to successfully modulate the performance of single-phase ceramics [16–22]. In the published work, heavy RE elements are generally selected to design the high-entropy RE_2SiO_5, such as $(Y_{1/4}Ho_{1/4}Er_{1/4}Yb_{1/4})_2SiO_5$ [23] and $(Yb_{1/4}Dy_{1/4}Ho_{1/4}Er_{1/4})_2SiO_5$ [24]. But they are difficult to achieve the improvement of thermal and mechanical properties synergistically. Reasonable composition is the key to the performance regulation of high-entropy ceramics. Previously, comprehensive studies have been conducted on the intrinsic thermal, mechanical, and corrosion resistance properties of RE_2SiO_5 ceramics [12,15,25]. The influence of RE elements on their properties has been understood clearly, which laid the theoretical foundation for the design of high-entropy RE_2SiO_5 ceramics.

Therefore, based on the aforementioned research, heavy RE elements Ho, Lu, and Yb, and light RE element Eu were chosen to design high-entropy $(Ho_{0.25}Lu_{0.25}Yb_{0.25}Eu_{0.25})_2SiO_5$. Lu and Yb are expected to provide excellent resistance to CMAS corrosion and low TEC. Ho can improve mechanical and thermal insulation properties. Eu could introduce oxygen vacancies to further reduce the thermal conductivity. The solid-station reaction method was applied to synthesize high-entropy $(Ho_{0.25}Lu_{0.25}Yb_{0.25}Eu_{0.25})_2SiO_5$. The phase composition, microstructure, lattice distortion, hardness, reduced modulus, TEC, thermal conductivity, and CMAS corrosion resistance of $(Ho_{0.25}Lu_{0.25}Yb_{0.25}Eu_{0.25})_2SiO_5$ were investigated synthetically. The results of this study reflect the excellent thermal insulation properties, suitable TEC, low reduced modulus, and good CMAS corrosion resistance of $(Ho_{0.25}Lu_{0.25}Yb_{0.25}Eu_{0.25})_2SiO_5$, which endow it a promising candidate for EBC.

2 Experimental

2. 1 Preparation of bulk $(Ho_{0.25}Lu_{0.25}Yb_{0.25}Eu_{0.25})_2SiO_5$

$(Ho_{0.25}Lu_{0.25}Yb_{0.25}Eu_{0.25})_2SiO_5$ powder was prepared by the solid-state reaction method. The raw materials are Ho_2O_3, Lu_2O_3, Yb_2O_3, Eu_2O_3 (> 99.9%; Jianfeng Co., Ltd., Guangzhou, China), and SiO_2 (99.7%; Sinopharm Chemical Reagent Co. Ltd., Shanghai, China). Firstly, Ho_2O_3, Lu_2O_3, Yb_2O_3, Eu_2O_3, and SiO_2 were mixed at a molar ratio of 1 : 1 : 1 : 1 : 4. Then, the mixture was ball-milled for 12 h by using ethyl alcohol as the medium. The obtained slurry was dried at 80 ℃ for 12 h, followed by passing through a 60-mesh sieve to get fine powder. The fine powder was sintered at 1650 ℃ for 8 h to get pure $(Ho_{0.25}Lu_{0.25}Yb_{0.25}Eu_{0.25})_2SiO_5$ powder. The as-prepared powder was ball-milled, dried, and sieved again. Then, it was made into a disc green body by uniaxially pressing at 5 MPa and cold isostatically pressing at 200 MPa for 15 min. Dense bulk $(Ho_{0.25}Lu_{0.25}Yb_{0.25}Eu_{0.25})_2SiO_5$ ceramic was fabricated by sintering the green body at 1550 ℃ for 12 h.

2. 2 Phase composition and microstructure

X-ray diffractometer (XRD, PANalytical Empyrean, Almero, the Netherlands) was applied to identify the phase composition. The Rietveld method in the General Structure Analysis System (GSAS) software was used for crystal structure refinement [26]. The scanning electron microscope (SEM, Hitachi, SU8230, Japan) equipped with an energy dispersive spectrometer (EDS) was used for microstructure observation and element distribution analysis. The stoichiometric ratio of reaction

products was identified by an electron probe micro-analyzer (EPMA, JEOL, JXA-8530F Plus, Japan). ImageJ software (open source) was used to analyze the grain size distribution, and at least 300 grains were counted. X-ray photoelectron spectrometer (XPS, Thermo Fisher, Nexsa, USA) was applied to analyze the chemical states of the elements of the specimen.

2. 3 Thermal and mechanical properties

The thermal diffusivity was measured by a laser flash analyzer (NETZSCH, LFA 427, Germany) from room temperature to 1000 ℃. The dimension of the specimen is 12.7 mm × 1 mm. Before the test, a graphite coating was applied to both sides of the specimen to reduce the effect of thermal radiation. The thermal conductivity (κ) was obtained from Eq. (1) [27]:

$$\kappa = \alpha \times \rho \times c_p \tag{1}$$

where ρ represents the density and c_p denotes the heat capacity. The heat capacity was calculated by the Neumann–Kopp law [28]. The thermal conductivity of a fully dense specimen (κ_0) is calculated by [29]:

$$\kappa_0 = \frac{\kappa}{1 - \frac{4\varphi}{3}} \tag{2}$$

where φ is the porosity.

The minimum thermal conductivity ($\kappa_{\min}$) was calculated by [30]:

$$\kappa_{\min} = 0.87\kappa_B \left(\frac{M}{n\rho N_A}\right)^{-\frac{2}{3}} \left(\frac{E}{\rho}\right)^{\frac{1}{2}} \tag{3}$$

where κ_B represents the Boltzmann constant, N_A denotes the Avogadro's constant, n is the number of atoms in the primitive cell, ρ is the density, E is the Young's modulus, and M is the molecular weight.

TEC was measured by an optical thermal expansion meter (ODHT, Modena, Italy) with a specimen dimension of 3 mm × 4 mm × 12 mm.

The reduced modulus and hardness characterization were performed by a nanoindenter (Bruker, Hysitron TI980, Germany). 400 points were taken in the range of 40 μm × 40 μm for measurement.

2. 4 CMAS corrosion

The composition of CMAS melt used in this work was 33CaO–9MgO–13$AlO_{1.5}$–45SiO_2, and the element proportion was expressed as molar ratios of single cationic oxides [31]. CaO, MgO, Al_2O_3, and SiO_2 were mixed according to the stoichiometric ratio of CMAS and a homogeneous mixture was obtained by wet ball milling for 12 h. The mixture was annealed at 1200 ℃ for 24 h, and then ball-milled, dried, and sieved again to obtain fine CMAS powder. Figure 1 shows a schematic diagram of the CMAS corrosion test procedure. The CMAS powder firstly was mixed with alcohol, and then they were uniformly coated on the sample surface. After several repeated coatings, the CMAS loading was kept at about 35 mg/cm^2. The CMAS-coated RE_2SiO_5 ceramic was heated at 1300 ℃ for 20 h. The heat-treated ceramic was cut along the midline for microstructure characterization.

3 Results and discussion

3. 1 Phase composition and microstructure

The reaction path of $(Ho_{0.25}Lu_{0.25}Yb_{0.25}Eu_{0.25})_2SiO_5$ was investigated by heating the mixed powder at different temperatures. Figure 2 presents the XRD patterns of the reaction products. RE_2O_3 does not react with SiO_2 until 1200 ℃. RE_2SiO_5 gradually appears with the increase of temperature, and a pure

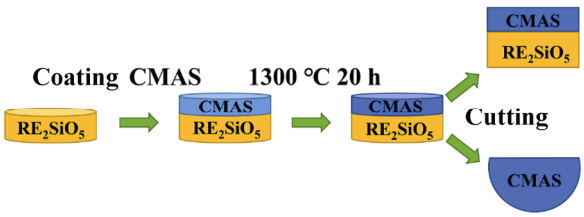

Fig. 1 Schematic of process of CMAS corrosion test.

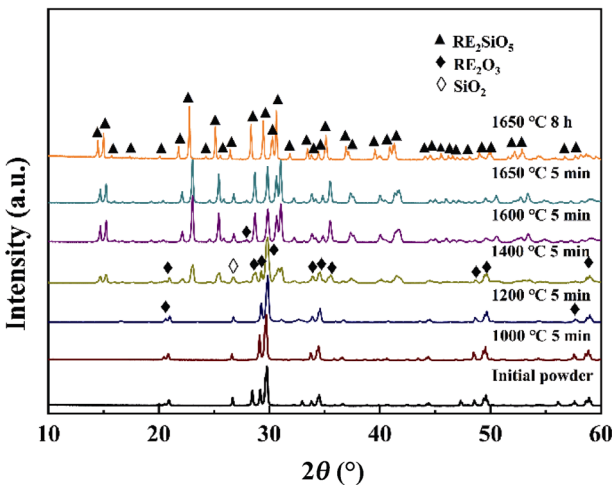

Fig. 2 XRD patterns of initial powder heated at different temperatures.

$(Ho_{0.25}Lu_{0.25}Yb_{0.25}Eu_{0.25})_2SiO_5$ phase can be obtained at 1650 ℃. The pure $(Ho_{0.25}Lu_{0.25}Yb_{0.25}Eu_{0.25})_2SiO_5$ powder was prepared at 1650 ℃ for 8 h to guarantee a complete reaction.

XRD patterns of $(Ho_{0.25}Lu_{0.25}Yb_{0.25}Eu_{0.25})_2SiO_5$ powder and mixed powder (a homogeneous mixture of Ho_2SiO_5, Lu_2SiO_5, Yb_2SiO_5, and Eu_2SiO_5 powder at 1 : 1 : 1 : 1 molar ratio) are compared and shown in Fig. 3. The X-ray diffraction peaks of $(Ho_{0.25}Lu_{0.25}Yb_{0.25}Eu_{0.25})_2SiO_5$ powder match well with the standard card of Lu_2SiO_5, indicating that the multiple RE elements have been successfully incorporated into the RE_2SiO_5 crystal lattice. Figures 3(b) and 3(c) display the enlarged XRD patterns in the diffraction angle ranges of 21°–24° and 27°–29°, respectively. The diffraction peaks of $(Ho_{0.25}Lu_{0.25}Yb_{0.25}Eu_{0.25})_2SiO_5$ shift to a lower angle compared to that of Lu_2SiO_5, since the radii of Ho^{3+}, Yb^{3+}, and Eu^{3+} are all larger than that of Lu^{3+}. For the mixed powder, it splits into four diffraction peaks which indicates that it is a mixture of four kinds of RE_2SiO_5 ceramics. Figure 4 exhibits the XRD pattern

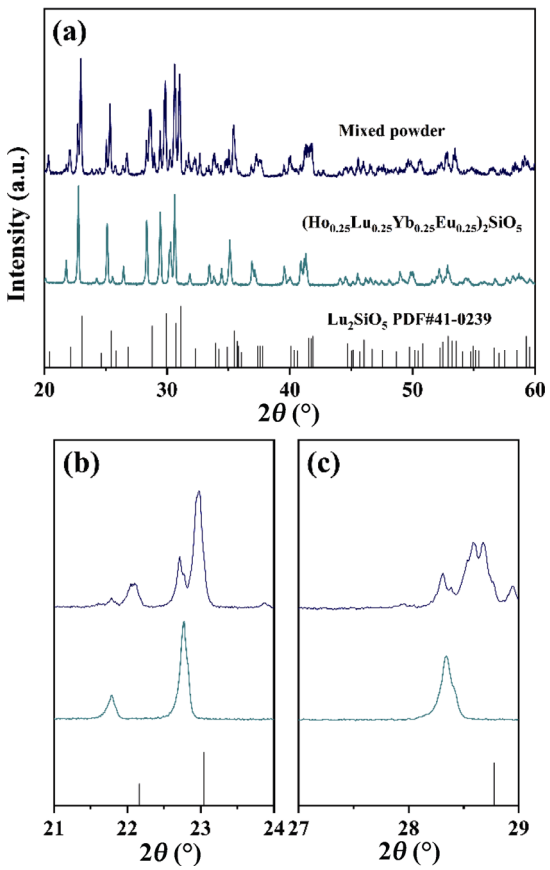

Fig. 3 (a) XRD patterns of $(Ho_{0.25}Lu_{0.25}Yb_{0.25}Eu_{0.25})_2SiO_5$ powder and mixed powder, (b) enlarged spectra of 21°–24°, and (c) enlarged spectra of 27°–29°.

of the bulk $(Ho_{0.25}Lu_{0.25}Yb_{0.25}Eu_{0.25})_2SiO_5$ ceramic, which maintains a pure phase with a small amount of $RE_2Si_2O_7$ impurities.

Rietveld refinement of X-ray diffraction data of $(Ho_{0.25}Lu_{0.25}Yb_{0.25}Eu_{0.25})_2SiO_5$ powder is shown in Fig. 5(a). The R_{wp} is 5.862%, and the goodness of fit (GOF) is 1.27, indicating that the refinement results are considered to be reliable. The lattice parameters of $(Ho_{0.25}Lu_{0.25}Yb_{0.25}Eu_{0.25})_2SiO_5$, Ho_2SiO_5, Lu_2SiO_5, Yb_2SiO_5, and Eu_2SiO_5 are listed in Table 1. $(Ho_{0.25}Lu_{0.25}Yb_{0.25}Eu_{0.25})_2SiO_5$ crystalizes in *C*2/*c* space group [32]. The lattice constant of $(Ho_{0.25}Lu_{0.25}Yb_{0.25}Eu_{0.25})_2SiO_5$ is between those of Ho_2SiO_5 and Yb_2SiO_5. Though Eu_2SiO_5 belongs to the X1-RE_2SiO_5 phase and crystalizes in the $P2_1/c$ space group, when combined with other RE elements to form a high-entropy ceramic, Eu atoms will occupy the RE lattice sites in X2-RE_2SiO_5. The theoretical density of $(Ho_{0.25}Lu_{0.25}Yb_{0.25}Eu_{0.25})_2SiO_5$ was calculated to be 6.83 g/cm^3, and the as-prepared specimen was measured with a porosity of 5%. The atomic occupation information is shown in Table 2. There are two independent RE sites (RE1 and RE2) in the X2-RE_2SiO_5 crystal structure (Fig. 5(b)). Small RE elements (Yb and Lu) tend to occupy the RE2 lattice position with a coordination number of 6, while large RE elements (Ho and Eu) prefer to occupy the RE1 lattice position with a coordination number of 7.

Figure 6 presents the surface morphology and elemental distribution of bulk $(Ho_{0.25}Lu_{0.25}Yb_{0.25}Eu_{0.25})_2SiO_5$ ceramic after thermally etching at 1300 ℃ for 30 min. Few cracks and pores can be found, which suggests that the as-prepared bulk $(Ho_{0.25}Lu_{0.25}Yb_{0.25}Eu_{0.25})_2SiO_5$ ceramic

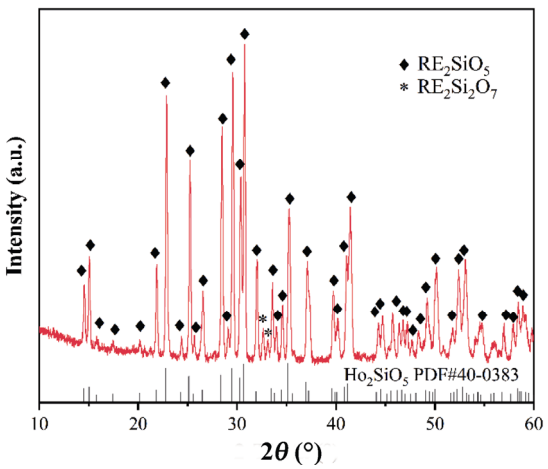

Fig. 4 XRD pattern of bulk $(Ho_{0.25}Lu_{0.25}Yb_{0.25}Eu_{0.25})_2SiO_5$ ceramic.

Table 1 Lattice structure parameters of $(Ho_{0.25}Lu_{0.25}Yb_{0.25}Eu_{0.25})_2SiO_5$, Ho_2SiO_5, Lu_2SiO_5, Yb_2SiO_5, and Eu_2SiO_5

Substance	$(Ho_{0.25}Lu_{0.25}Yb_{0.25}Eu_{0.25})_2SiO_5$	Ho_2SiO_5	Lu_2SiO_5	Yb_2SiO_5	Eu_2SiO_5
Space group	*C*2/*c*	*C*2/*c*	*C*2/*c*	*C*2/*c*	$P2_1/c$
a (Å)	14.40	14.48	14.33	14.37	9.15
b (Å)	6.73	6.76	6.67	6.69	6.76
c (Å)	10.44	10.47	10.32	10.34	7.08
α (°)	90	90	90	90	90
β (°)	122.15	122.23	122.30	122.78	107.82
Volume ($Å^3$)	856.69	866.94	834.89	836.12	416.96
Theoretical density (g/cm^3)	6.83	6.71	7.30	7.22	6.56

Table 2 Atomic occupation of $(Ho_{0.25}Lu_{0.25}Yb_{0.25}Eu_{0.25})_2SiO_5$

Site	Element	Wyckoff symbol	*X*	*Y*	*Z*	Fraction
Ho1	Ho	8f	0.46246	0.24448	0.53350	0.3216
Lu1	Lu	8f	0.46246	0.24448	0.53350	0.1445
Yb1	Yb	8f	0.46246	0.24448	0.53350	0.1636
Eu1	Eu	8f	0.46246	0.24448	0.53350	0.3704
Ho2	Ho	8f	0.35851	0.12336	0.16567	0.1784
Lu2	Lu	8f	0.35851	0.12336	0.16567	0.3555
Yb2	Yb	8f	0.35851	0.12336	0.16567	0.3364
Eu2	Eu	8f	0.35851	0.12336	0.16567	0.1296
Si	Si	8f	0.18400	0.08600	0.30400	1.0000
O1	O	8f	0.12600	0.28700	0.33400	1.0000
O2	O	8f	0.09300	0.00800	0.15600	1.0000
O3	O	8f	0.29600	0.12800	0.32500	1.0000
O4	O	8f	0.31200	0.40600	0.09600	1.0000
O5	O	8f	0.48100	0.08500	0.10600	1.0000

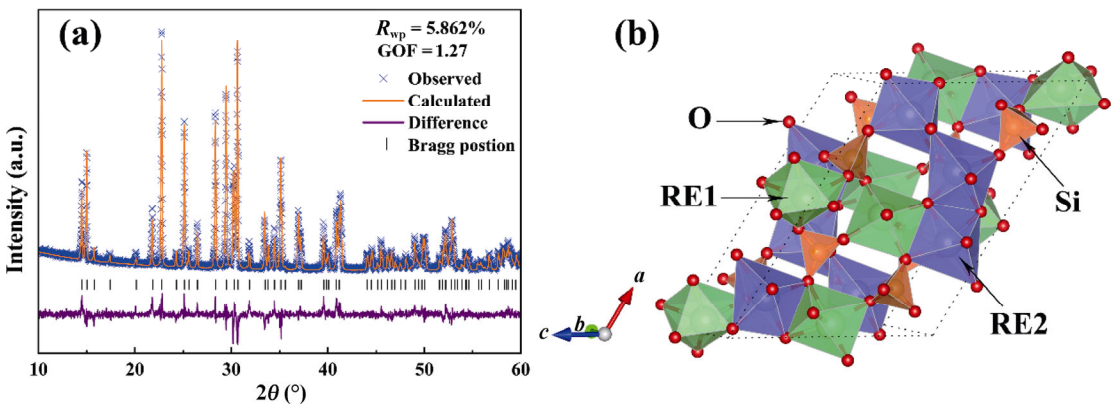

Fig. 5 (a) Rietveld refinement of XRD pattern and (b) crystal structure of $(Ho_{0.25}Lu0_{.25}Yb_{0.25}Eu_{0.25})_2SiO_5$.

is relatively dense. The four RE elements are distributed homogeneously, while some areas are rich in silicon. The point analysis of each region is summarized in Table 3. In the silicon enriched area (point 2), the ratio of RE to Si is about 1 : 1, which proves to be $RE_2Si_2O_7$ impurities.

Table 3 SEM–EDS point analysis of bulk $(Ho_{0.25}Lu_{0.25}Yb_{0.25}Eu_{0.25})_2SiO_5$ ceramic

(Unit: mol%)

Point	Ho	Lu	Yb	Eu	Si	O
1	7.16	6.70	7.30	7.07	12.65	59.12
2	5.49	5.32	5.55	4.37	21.63	57.64

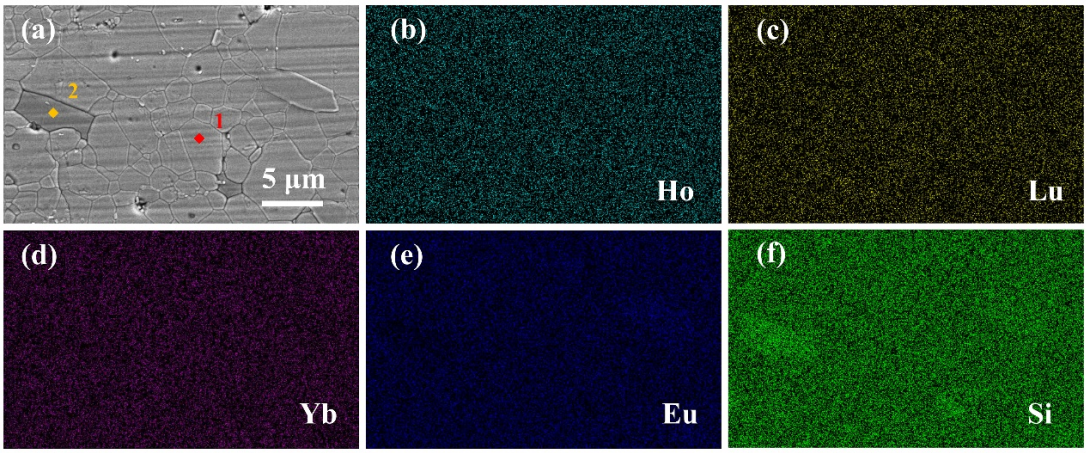

Fig. 6 (a) Surface morphology, and (b)–(f) EDS mappings of Ho, Lu, Yb, Eu, and Si, respectively.

3. 2 Thermal properties

Thermal properties are important parameters for EBC. Figure 7(a) compares the thermal diffusivities of $(Ho_{0.25}Lu_{0.25}Yb_{0.25}Eu_{0.25})_2SiO_5$, Ho_2SiO_5, Lu_2SiO_5, Yb_2SiO_5, and Eu_2SiO_5 [15,25]. They generally decrease with the increase of temperature but increase slightly under the influence of thermal radiation at high temperatures [33]. This phenomenon is particularly evident in Lu_2SiO_5. $(Ho_{0.25}Lu_{0.25}Yb_{0.25}Eu_{0.25})_2SiO_5$ exhibits the lowest thermal diffusivity above 400 ℃. When the temperature exceeds 200 ℃, the thermal diffusivity of $(Ho_{0.25}Lu_{0.25}Yb_{0.25}Eu_{0.25})_2SiO_5$ is about half that of Lu_2SiO_5. Figure 7(b) displays the thermal conductivities calculated by Eqs. (1) and (2). They decrease with the increase of temperature and increase slightly at high temperatures, which is caused by the thermal radiation [33]. $(Ho_{0.25}Lu_{0.25}Yb_{0.25}Eu_{0.25})_2SiO_5$ possesses very low thermal conductivity in the range of 1.07–1.47 $W\cdot m^{-1}\cdot K^{-1}$. From room temperature to 800 ℃, the thermal conductivity of $(Ho_{0.25}Lu_{0.25}Yb_{0.25}Eu_{0.25})_2SiO_5$ is the lowest among Ho_2SiO_5, Lu_2SiO_5, Yb_2SiO_5, and Eu_2SiO_5. The κ_{min} of $(Ho_{0.25}Lu_{0.25}Yb_{0.25}Eu_{0.25})_2SiO_5$ is 0.99 $W\cdot m^{-1}\cdot K^{-1}$, which is lower than those of Ho_2SiO_5 (1.01 $W\cdot m^{-1}\cdot K^{-1}$), Lu_2SiO_5 (1.05 $W\cdot m^{-1}\cdot K^{-1}$), Yb_2SiO_5 (1.01 $W\cdot m^{-1}\cdot K^{-1}$) [15], and Eu_2SiO_5 (1.01 $W\cdot m^{-1}\cdot K^{-1}$) [25]. In Fig. 7(b), the thermal conductivity of $(Ho_{0.25}Lu_{0.25}Yb_{0.25}Eu_{0.25})_2SiO_5$ is very close to its minimum thermal conductivity from room temperature to 1000 ℃. Eu_2SiO_5 also presents a low thermal conductivity in the whole temperature range, but it is not an EBC candidate. Thermal conductivities of RE_2SiO_5 (RE = Ho, Lu, and Yb) present a rapid decrease with the temperature rising, and they approach the minimum thermal conductivity under the synergy of severe phonon scattering and thermal radiation. Therefore, $(Ho_{0.25}Lu_{0.25}Yb_{0.25}Eu_{0.25})_2SiO_5$ maintains a low thermal conductivity compared to RE_2SiO_5 (RE = Ho, Lu, Yb, and Eu), and its thermal conductivity is close to its limit at high temperatures, which show advantages as EBC candidate. To reveal the factors that dominate the low thermal conductivity of $(Ho_{0.25}Lu_{0.25}Yb_{0.25}Eu_{0.25})_2SiO_5$, the phonon scattering mechanism was analyzed in detail.

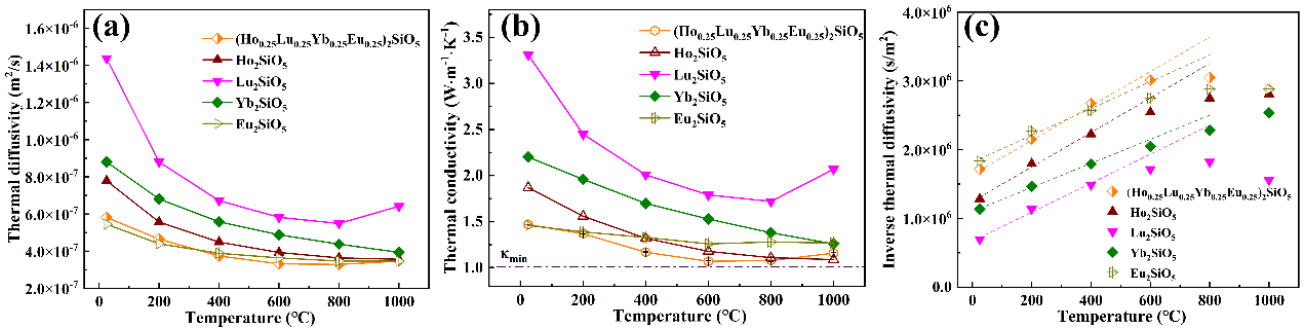

Fig. 7 (a) Thermal diffusivities, (b) thermal conductivities, and (c) inverse thermal diffusivities of $(Ho_{0.25}Lu_{0.25}Yb_{0.25}Eu_{0.25})_2SiO_5$, Ho_2SiO_5, Lu_2SiO_5, Yb_2SiO_5, and Eu_2SiO_5.

In thermal insulation materials, the propagation of phonons determines thermal conductivity [33]. According to the Debye model, the thermal diffusivity is defined as [34]:

$$\alpha = \frac{1}{3} v_{\mathrm{m}} \Lambda \tag{4}$$

where v_{m} denotes the average sound velocity, Λ represents the mean free path of phonon, and Λ can be expressed as [35]:

$$\frac{1}{\Lambda} = \frac{1}{\Lambda_{\mathrm{phonon}}} + \frac{1}{\Lambda_{\mathrm{defect}}} + \frac{1}{\Lambda_{\mathrm{boundary}}} + \sum_i \frac{1}{\Lambda_i} \tag{5}$$

where $\Lambda_{\mathrm{phonon}}$ denotes the mean free path of phonon determined by the phonon Umklapp scattering, $\Lambda_{\mathrm{defect}}$ corresponds to the phonon–defect scattering, $\Lambda_{\mathrm{boundary}}$ is related to the phonon–boundary scattering, and Λ_i is affected by other scattering mechanisms. Among $\Lambda_{\mathrm{phonon}}$, $\Lambda_{\mathrm{defect}}$, $\Lambda_{\mathrm{boundary}}$, and Λ_i, only $\Lambda_{\mathrm{phonon}}$ is closely related to temperature, and thus $\Lambda_{\mathrm{phonon}}$ dominates the variation of Λ with temperature [27, 36]. $\Lambda_{\mathrm{phonon}}$ represents the intrinsic heat conduction of the materials, while $\Lambda_{\mathrm{defect}}$, $\Lambda_{\mathrm{boundary}}$, and Λ_i are caused by external factors.

In crystalline materials, the mean free path of phonon is defined as [35]:

$$\Lambda = \Lambda_0 \left(\exp\left(\frac{\theta_{\mathrm{D}}}{bTn^{\frac{1}{3}}} \right) - 1 \right) \tag{6}$$

where Λ_0 represents the pre-exponential factor, the constant b is approximately equal to 2, θ_{D} denotes the Debye temperature, and n represents the number of atoms in the unit cell. In the high-temperature stage, Λ^{-1} can be estimated as [33]:

$$\frac{1}{\Lambda} \sim \frac{C}{\exp\left(\frac{\theta_{\mathrm{D}}}{bTn^{\frac{1}{3}}} \right) - 1} + D = \left(\frac{bCn^{\frac{1}{3}}}{\theta_{\mathrm{D}}} \right) T + \left(D - \frac{1}{2} C \right) \tag{7}$$

Equation (7) exhibits that Λ^{-1} and temperature T are linearly correlated. Whereas in Eq. (4), the average sound velocity v_{m} is almost independent of temperature, and thus there is also a linear relationship between thermal diffusivity and temperature [33]:

$$\frac{1}{\Lambda} \sim \frac{1}{\alpha} \sim \left(\frac{bCn^{\frac{1}{3}}}{\theta_{\mathrm{D}}} \right) T + \left(D - \frac{1}{2} C \right) \tag{8}$$

The temperature-dependent part of Eq. (8) is the slope which is determined by phonon–phonon scattering, and the temperature-independent part is the intercept which is determined by external factors such as defects [37].

The relationship of the inverse thermal diffusivity α^{-1} versus temperature T is shown in Fig. 7(c). From room temperature to 400 ℃, α^{-1} increases linearly with the increase of temperature. When the temperature exceeds 400 ℃, it deviates from the linear relationship due to thermal radiation. The expressions, slopes, and intercepts of the linear relationship of the inverse thermal diffusivity α^{-1} versus temperature T are listed in Table 4. According to Eq. (8), a larger intercept indicates a greater concentration of point defects [37]. For $(Ho_{0.25}Lu_{0.25}Yb_{0.25}Eu_{0.25})_2SiO_5$, its intercept is the second largest indicating a high concentration of defects that contribute to the low thermal conductivity.

For materials with defects, the thermal conductivity is inversely proportional to the square root of the phonon scattering coefficient. According to the elastic continuum medium model, Wan *et al*. [38] defined a method of quantifying the phonon scattering coefficient based on the effective elastic properties of the matrix and the effective ionic radius of the defect:

$$\Gamma_i = f_i \left\{ \left(\frac{\Delta M_i}{M} \right)^2 + 2 \left[6.4 \times \frac{1}{3} \gamma \frac{1+\nu}{1-\nu} \left(\frac{\Delta \delta_i}{\delta} \right) \right]^2 \right\} \tag{9}$$

where the subscript i denotes a certain lattice defect, f_i denotes the concentration of this defect, $\Delta M_i = M - M_i$, $\Delta \delta_i = \delta - \delta_i$, M_i and δ_i represent the atomic mass and the ionic radius of the specific defect, respectively, γ is the Grüneisen parameter, which represents the anharmonic vibrations within the whole lattice, and ν is the Poisson ratio. Based on Eq. (9), it is known that, the mismatch of atomic masses and ionic radii of several RE elements in $(Ho_{0.25}Lu_{0.25}Yb_{0.25}Eu_{0.25})_2SiO_5$ leads to an increase in the phonon scattering coefficient and thus a decrease in the thermal conductivity.

Table 4 Parameters of the linear fit of the inverse thermal diffusivities [15,25]

Material	α^{-1}	Slope	Intercept
$(Ho_{0.25}Lu_{0.25}Yb_{0.25}Eu_{0.25})_2SiO_5$	$2550T + 953150$	2550	953150
Ho_2SiO_5	$2510T + 561420$	2510	561420
Lu_2SiO_5	$2110T + 92390$	2110	92390
Yb_2SiO_5	$1750T + 623120$	1750	623120
Eu_2SiO_5	$1950T + 1286700$	1950	1286700

In addition, because the outer electron structure of the Eu is $4f^7 6s^2$, when it loses two electrons, the outer electron structure is $4f^7$. $4f^7$ is half-filled, which is also a stable state according to Hundt's rule. Therefore, Eu^{2+} may exist in $(Ho_{0.25}Lu_{0.25}Yb_{0.25}Eu_{0.25})_2SiO_5$, thereby promoting the generation of oxygen vacancies which can dramatically decrease the thermal conductivity.

XPS analysis was used to further investigate the valence state of the elements in $(Ho_{0.25}Lu_{0.25}Yb_{0.25}Eu_{0.25})_2SiO_5$. Figure 8(a) is the XPS spectrum of Ho 4d. Three peaks are located at 160.97, 163.13, and 167.06 eV. They correspond to the Ho^{3+} $4d_{5/2}$, Ho^{3+} $4d_{3/2}$, and Ho^{3+} $4d_{5/2}$, respectively. In Fig. 8(b), two peaks are determined at 196.73 and 206.46 eV, which belong to Lu^{3+} $4d_{5/2}$ and Lu^{3+} $4d_{3/2}$, respectively. Figure 8(c) exhibits the XPS spectrum of Yb 4d, and there are two weak peaks located at 185.64 and 189.21 eV, which correspond to Yb^{3+} $4d_{5/2}$ and Yb^{3+} $4d_{3/2}$, respectively. Figure 8(d) is the XPS spectrum of Eu 3d, and there are four peaks located at 1125.69, 1134.90, 1155.49, and 1164.87 eV. The peaks at 1134.90 and 1164.87 eV correspond to Eu^{3+} $3d_{5/2}$ and Eu^{3+} $3d_{3/2}$, respectively, and the peaks at 1125.69 and 1155.49 eV belong to Eu^{2+} $3d_{5/2}$ and Eu^{2+} $3d_{3/2}$, respectively. In $(Ho_{0.25}Lu_{0.25}Yb_{0.25}Eu_{0.25})_2SiO_5$, Ho, Lu, and Yb are in 3+ valence state, and Eu has two valence states, Eu^{2+} and Eu^{3+}. For the charge balance, oxygen vacancies tend to be generated in $(Ho_{0.25}Lu_{0.25}Yb_{0.25}Eu_{0.25})_2SiO_5$, which can enhance the scattering of phonons, resulting in a decrease in thermal conductivity. Typically speaking, the oxygen vacancies may lead to the high oxygen ion conductivity of the TBC or EBC, resulting in the accelerated oxidation of the bond coat. It has been found that, two main factors dominate the oxygen ionic conductivity of oxide ceramics: the oxygen vacancies and the activation energy of oxygen migration [39]. As shown in Fig. 8(d), the content of Eu^{2+} is not high; therefore, the number of oxygen vacancies originating from the Eu element is not large. The activation energy of oxygen migration in $(Ho_{0.25}Lu_{0.25}Yb_{0.25}Eu_{0.25})_2SiO_5$ is controlled mainly by the strength of RE–O bonds. It suggests that a smaller radius of RE^{3+} presents higher activation energy of oxygen ion migration. In $(Ho_{0.25}Lu_{0.25}Yb_{0.25}Eu_{0.25})_2SiO_5$, the ionic radii of Ho, Yb, and Lu are small, and the oxygen diffusion rate should not be high. In addition, Matsudaira *et al*. [40] evaluated the oxygen diffusion in Yb_2SiO_5. The results confirm that oxide ion diffuses more preferentially along the grain boundary than the interior of the grain. Therefore, oxygen vacancies introduced by Eu^{2+} in $(Ho_{0.25}Lu_{0.25}Yb_{0.25}Eu_{0.25})_2SiO_5$ should not lead to a significant effect on the oxidation of the bond coat.

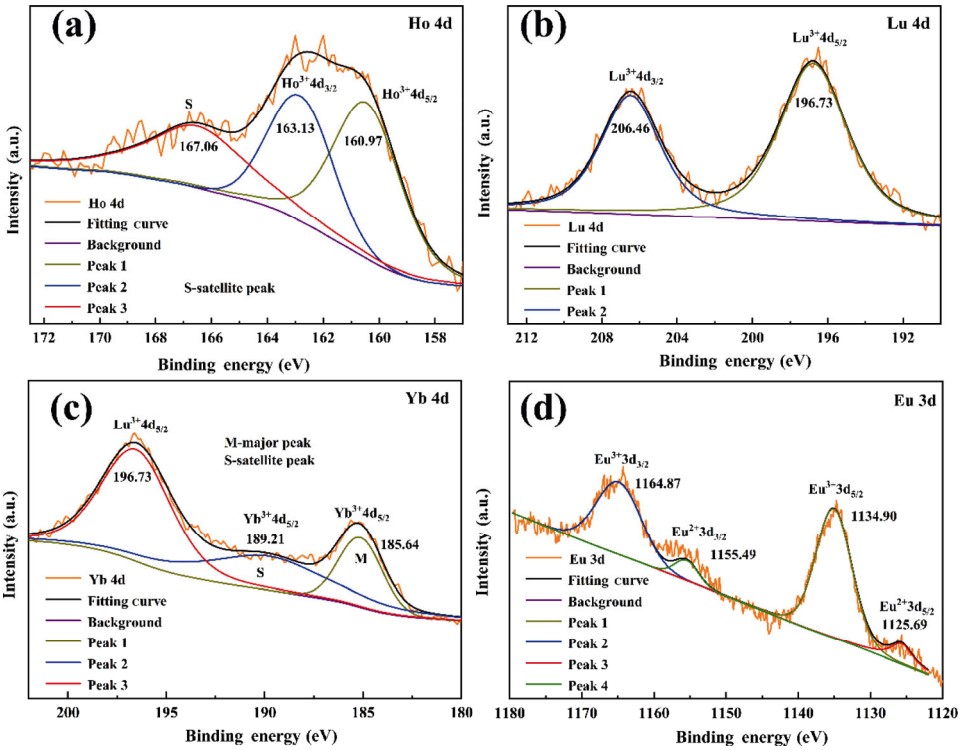

Fig. 8 XPS spectra of (a) Ho 4d, (b) Lu 4d, (c) Yb 4d, and (d) Eu 3d of $(Ho_{0.25}Lu_{0.25}Yb_{0.25}Eu_{0.25})_2SiO_5$.

As EBC materials, the TEC is required to match with the substrate to release the thermal stress between the coating and the substrate during thermal cycling [6]. The TEC of $(Ho_{0.25}Lu_{0.25}Yb_{0.25}Eu_{0.25})_2SiO_5$ was measured and compared with RE_2SiO_5 (RE = Ho, Lu, Yb, and Eu), some high-entropy RE_2SiO_5, and SiC (Fig. 9) [15, 23–25]. $(Ho_{0.25}Lu_{0.25}Yb_{0.25}Eu_{0.25})_2SiO_5$ displays lower TEC than the single-phase RE_2SiO_5 ceramics, and it is comparable to those of $(Y_{0.25}Ho_{0.25}Er_{0.25}Yb_{0.25})_2SiO_5$ and $(Yb_{0.25}Dy_{0.25}Ho_{0.25}Er_{0.25})_2SiO_5$. The TEC of $(Ho_{0.25}Lu_{0.25}Yb_{0.25}Eu_{0.25})_2SiO_5$ is in the range of (4.0–5.9)×10^{-6} K^{-1} which is close to that of SiC ((4.5–5.5)×10^{-6} K^{-1}) [41]. Although there is a very small amount of $RE_2Si_2O_7$ in the specimen, Nasiri *et al.* [42] suggested that $RE_2Si_2O_7$ impurities have little contribution to thermal expansion. They prepared RE_2SiO_5 (RE = Gd, Yb, Lu) ceramics containing $RE_2Si_2O_7$ impurities. But the TECs of Gd_2SiO_5, Yb_2SiO_5, and Lu_2SiO_5 are (10.3±0.4)×10^{-6} K^{-1}, (7.2±0.5)×10^{-6} K^{-1}, and (6.7±0.6)×10^{-6} K^{-1}, respectively, which not show a significant decrease in TEC. Therefore, $RE_2Si_2O_7$ impurities do not contribute much to thermal expansion.

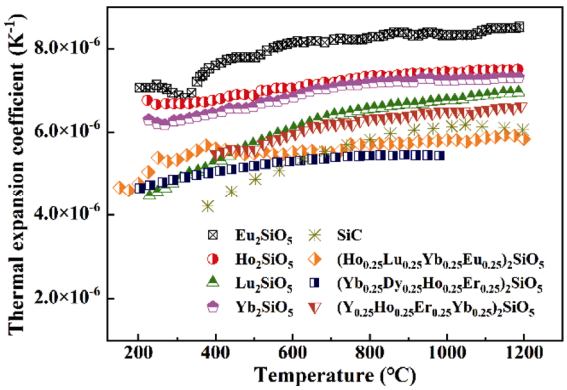

Fig. 9 TECs of $(Ho_{0.25}Lu_{0.25}Yb_{0.25}Eu_{0.25})_2SiO_5$, Ho_2SiO_5, Lu_2SiO_5, Yb_2SiO_5, Eu_2SiO_5, $(Yb_{0.25}Dy_{0.25}Ho_{0.25}Er_{0.25})_2SiO_5$, $(Y_{0.25}Ho_{0.25}Er_{0.25}Yb_{0.25})_2SiO_5$, and SiC.

It has been found that, there are two species of phonons with different signs of Grüneisen constant in X2-RE_2SiO_5. One type of phonon has a positive Grüneisen constant and contributes to positive thermal expansion, and the other has a negative Grüneisen constant and contributes to negative thermal expansion [43]. According to the crystal structure, $(Ho_{0.25}Lu_{0.25}Yb_{0.25}Eu_{0.25})_2SiO_5$, Ho_2SiO_5, Lu_2SiO_5, and Yb_2SiO_5 belong to the X2 phase, and they consist of [REO_7], [REO_6] polyhedra, and [SiO_4] tetrahedra [15]. Eu_2SiO_5 belongs to the X1 phase which consists of [REO_7], [REO_9] polyhedra, and [SiO_4] tetrahedra [25]. The lattice distortion was calculated separately for [REO_7], [REO_6], [REO_9] polyhedra, and [SiO_4] tetrahedra by the bond lengths [44]:

$$\Delta_d = \frac{1}{n}\sum_n \left(\frac{d(\mathrm{L-O})_n - \overline{d(\mathrm{L-O})}}{\overline{d(\mathrm{L-O})}} \right)^2 \qquad (10)$$

where Δ_d is the degree of lattice distortion, $d(\mathrm{L-O})$ represents the bond length between the RE or Si atom and the nth O atom, and $\overline{d(\mathrm{L-O})}$ represents the average bond length between them. In Table 5, we can see that $(Ho_{0.25}Lu_{0.25}Yb_{0.25}Eu_{0.25})_2SiO_5$ shows the

Table 5 Degree of distortion of [REO_7], [REO_6], [REO_9] polyhedra, and [SiO_4] tetrahedra of $(Ho_{0.25}Lu_{0.25}Yb_{0.25}Eu_{0.25})_2SiO_5$, Ho_2SiO_5, Lu_2SiO_5, Yb_2SiO_5, and Eu_2SiO_5

Compound	Bond	Polyhedra	Bond length (Å)							Average bond length (Å)	Degree of distortion (‰)
$(Ho_{0.25}Lu_{0.25}Yb_{0.25}Eu_{0.25})_2SiO_5$	RE1–O	[REO_7]	2.452	2.280	2.355	2.312	2.321	2.336	2.751	2.401	3.975
	RE2–O	[REO_6]	2.177	2.274	2.286	2.528	2.019	2.274		2.260	4.499
	Si–O	[SiO_4]	1.704	1.492	1.534	1.580				1.578	2.531
Ho_2SiO_5	RE1–O	[REO_7]	2.301	2.145	2.342	2.585	2.394	2.253	2.377	2.342	2.901
	RE2–O	[REO_6]	2.223	2.253	2.278	2.265	2.237	2.312		2.261	0.163
	Si–O	[SiO_4]	1.624	1.619	1.650	1.627				1.630	0.053
Lu_2SiO_5	RE1–O	[REO_7]	2.319	2.235	2.124	2.281	2.370	2.354	2.562	2.321	2.901
	RE2–O	[REO_6]	2.235	2.289	2.243	2.203	2.219	2.256		2.241	0.149
	Si–O	[SiO_4]	1.609	1.604	1.634	1.614				1.615	0.050
Yb_2SiO_5	RE1–O	[REO_7]	2.292	2.331	2.380	2.558	2.233	2.145	2.387	2.332	2.700
	RE2–O	[REO_6]	2.259	2.215	2.269	2.314	2.228	2.230		2.253	0.217
	Si–O	[SiO_4]	1.608	1.618	1.643	1.627				1.624	0.063
Eu_2SiO_5	RE1–O	[REO_7]	2.312	2.387	2.300	2.404	2.309	2.508	2.546	2.395	1.470
	RE2–O	[REO_9]	2.347 2.283	2.423 2.766	2.517	2.697	2.356	2.562	2.503	2.495	3.760
	Si–O	[SiO_4]	1.675	1.633	1.605	1.633				1.637	0.233

highest degree of lattice distortion. The severe lattice distortion and inhomogeneous bond length of $(Ho_{0.25}Lu_{0.25}Yb_{0.25}Eu_{0.25})_2SiO_5$ may change the anharmonicity of low-frequency phonons, which leads to the increase of the content of phonons with negative Grüneisen constant [23]. Therefore, the TEC of $(Ho_{0.25}Lu_{0.25}Yb_{0.25}Eu_{0.25})_2SiO_5$ is lower than those of RE_2SiO_5 (RE = Ho, Lu, Yb, and Eu).

3. 3 Mechanical properties

In addition to the TEC, the elastic modulus and hardness are also critical parameters of EBC [25]. Figures 10(a) and 10(b) exhibit the mappings of reduced moduli and hardness of $(Ho_{0.25}Lu_{0.25}Yb_{0.25}Eu_{0.25})_2SiO_5$ ceramic measured by nanoindentation. Figures 10(c) and 10(d) display the distribution statistics of the reduced moduli and hardness, respectively. The reduced modulus can be approximately equal to Young's modulus [45]. The values of reduced moduli and hardness of $(Ho_{0.25}Lu_{0.25}Yb_{0.25}Eu_{0.25})_2SiO_5$ and RE_2SiO_5 (RE = Ho, Lu, Yb, and Eu) are summarized in Table 6. The reduced modulus of $(Ho_{0.25}Lu_{0.25}Yb_{0.25}Eu_{0.25})_2SiO_5$ is lower than those of Lu_2SiO_5 and Yb_2SiO_5 but higher than the reduced moduli of Ho_2SiO_5 and Eu_2SiO_5. Also, the hardness of $(Ho_{0.25}Lu_{0.25}Yb_{0.25}Eu_{0.25})_2SiO_5$ is comparable with those of RE_2SiO_5 (RE = Ho, Lu, Yb, and Eu). Young's modulus of ceramic is related to the bond strengths which can be represented by the cation field strength (CFS) [46]. CFS can be calculated by using the equation: CFS = Z_c/r_c^2, where Z_c is the cationic charge, and r_c is the cationic radius. Therefore, Eu^{3+} and Ho^{3+} with larger radii contribute to the relatively low reduced modulus of $(Ho_{0.25}Lu_{0.25}Yb_{0.25}Eu_{0.25})_2SiO_5$. Also, the synergistic effect of the four RE elements leads to the reduced modulus of $(Ho_{0.25}Lu_{0.25}Yb_{0.25}Eu_{0.25})_2SiO_5$ lower than the average value of the four RE_2SiO_5 (Fig. 15).

Table 6 Reduced moduli and hardness of $(Ho_{0.25}Lu_{0.25}Yb_{0.25}Eu_{0.25})_2SiO_5$, Ho_2SiO_5, Lu_2SiO_5, Yb_2SiO_5, and Eu_2SiO_5

Material	Reduced modulus (GPa)	Hardness (GPa)
$(Ho_{0.25}Lu_{0.25}Yb_{0.25}Eu_{0.25})_2SiO_5$	149.0±16.5	11.7±2.1
Ho_2SiO_5	146.0±10.1	11.7±1.2
Lu_2SiO_5	156.2±14.0	12.8±1.6
Yb_2SiO_5	164.1±14.1	12.2±1.8
Eu_2SiO_5	147.0±19.2	11.3±2.9

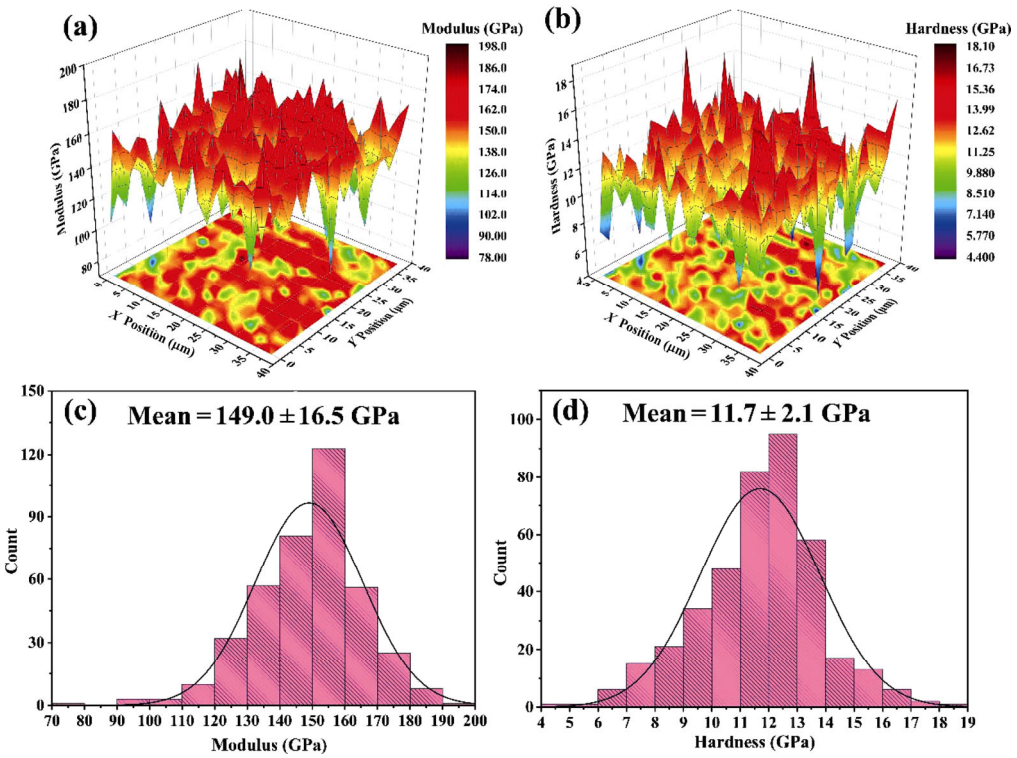

Fig. 10 (a, b) Nanoindentation mappings of reduced moduli and hardness, respectively, and (c, d) distribution statistics of reduced moduli and hardness of $(Ho_{0.25}Lu_{0.25}Yb_{0.25}Eu_{0.25})_2SiO_5$, respectively.

3. 4 CMAS corrosion

The turbine blade in the gas turbine engines usually suffers from severe hot corrosion by debris (such as dust, sand, and ash), which is generically known as CMAS corrosion [5]. A high-temperature CMAS corrosion test was performed to evaluate the resistance of corrosion. Figure 11(a) displays the surface morphology of $(Ho_{0.25}Lu_{0.25}Yb_{0.25}Eu_{0.25})_2SiO_5$ after the CMAS corrosion at 1300 ℃ for 20 h. Some reaction products can be observed to be immersed in the CMAS melt. Figure 11(b) shows the XRD pattern of $(Ho_{0.25}Lu_{0.25}Yb_{0.25}Eu_{0.25})_2SiO_5$ after corrosion. RE silicate oxyapatite $Ca_2RE_8(SiO_4)_6O_2$ and garnet-type phase are the main reaction products [12]. Figure 12(a) exhibits the microstructure of the cross-section of the specimen. The infiltration depth is determined to be 125.4 ± 8.7 μm. Figure 12(b) displays the cross-section image at higher magnification, and Figs. 12(c)–12(h) presents the EDS element mappings. The cross-section can be divided into three layers. The top layer which is rich in Ca and Si elements and less in RE elements is the residual CMAS melt. The middle layer with a large number of rod-like grains is the reaction zone. Besides the rod-like grains, there are also large gray regions where Ca and Si contents are relatively low, with a certain amount of RE elements (Fig. 13). The bottom is $(Ho_{0.25}Lu_{0.25}Yb_{0.25}Eu_{0.25})_2SiO_5$ high-entropy ceramic.

The compositions of reaction products analyzed by EPMA are summarized in Table 7. The top layer with a low content of RE elements is residual CMAS melt (point A). The ratio of Ca to RE elements of the rod-like grains is about 1 : 4, which can be identified

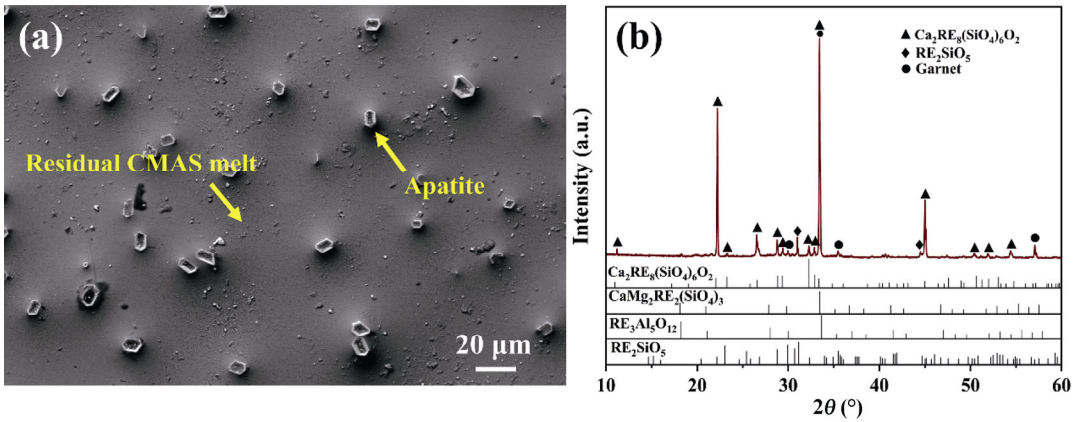

Fig. 11 (a) Surface morphology and (b) XRD pattern of $(Ho_{0.25}Lu_{0.25}Yb_{0.25}Eu_{0.25})_2SiO_5$ after CMAS corrosion at 1300 ℃ for 20 h.

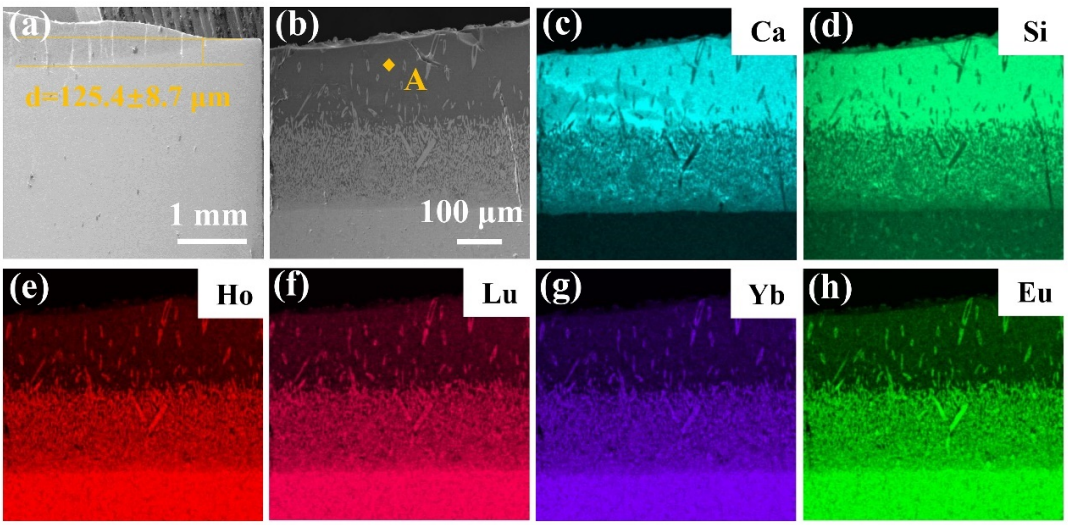

Fig. 12 (a, b) Cross-sectional morphology of $(Ho_{0.25}Lu_{0.25}Yb_{0.25}Eu_{0.25})_2SiO_5$ after CMAS corrosion at 1300 ℃ for 20 h. (c)–(h) EDS element mappings of Ca, Si, Ho, Lu, Yb, and Eu of (b), respectively.

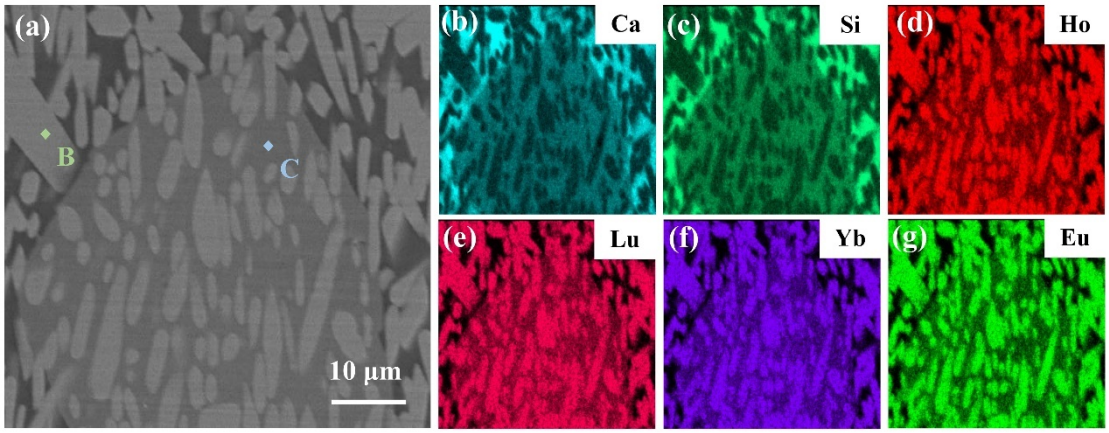

Fig. 13 (a) High-magnification cross-sectional morphology of $(Ho_{0.25}Lu_{0.25}Yb_{0.25}Eu_{0.25})_2SiO_5$ after CMAS corrosion at 1300 ℃ for 20 h. (b)–(g) EDS element mappings of Ca, Si, Ho, Lu, Yb, and Eu of (a), respectively.

Table 7 EPMA point analysis of the cross-section of $(Ho_{0.25}Lu_{0.25}Yb_{0.25}Eu_{0.25})_2SiO_5$ after CMAS corrosion at 1300 ℃ for 20 h

(Unit: mol%)

Point	CaO	MgO	$AlO_{1.5}$	SiO_2	$HoO_{1.5}$	$LuO_{1.5}$	$YbO_{1.5}$	$EuO_{1.5}$
A	23.40	18.63	8.85	43.48	1.13	1.82	1.51	1.18
B	12.19	1.28	0.00	36.63	12.93	11.04	9.43	16.50
C	16.89	22.41	6.64	37.29	3.90	5.01	4.41	3.45

as apatite $Ca_2RE_8(SiO_4)_6O_2$ (point B). The large gray region contains Ca, Mg, Al, Si, and RE (point C) which may be the other reaction products in a garnet-type phase. $Y_3Al_5O_{12}$ is one of the typical garnet-type phases. The large gray region contains Ca, Mg, Al, Si, and RE, and the ratio of (Ca + RE) : (Mg + Al + Si) is about 3 : 5, which indicates that it may be a garnet-type phase. According to the literature, the composition of garnet-type phases can be very complex, such as $MgY_2Al_4SiO_{12}$ [47], $Li_{7+2x-y}(La_{3-x}Rb_x)(Zr_{2-y}Ta_y)O_{12}$ [48], $Y_{2.8-x}Dy_{0.2}Ce_xFe_5O_{12}$ [49], etc. Therefore, the chemical formula of the garnet-type phase in the reaction zone should be $(Ca_xRE_{3-x})(Mg_yAl_zSi_{5-y-z})O_{12}$.

According to the reaction products, the following reactions should occur during the CMAS corrosion process:

$$4RE_2SiO_5+2CaO+2SiO_2 \rightarrow Ca_2RE_8(SiO_4)_6O_2 \quad (11)$$

$$xCaO + yMgO + zAl_2O_3 + \left(\frac{7+x}{2} - y - z\right)SiO_2 + \left(\frac{3-x}{2}\right)RE_2SiO_5 \rightarrow (Ca_xRE_{3-x})(Mg_yAl_zSi_{5-y-z})O_{12} \quad (12)$$

The interaction between CMAS and RE_2SiO_5 (RE = Ho, Lu, Yb, and Eu) has been performed, and their CMAS infiltration depths are 166.5±23.6 μm, 40.2 ± 3.2 μm, 75.1±2.0 μm, and 248.6±14.3 μm, respectively (Fig. 14). The CMAS infiltration depth of $(Ho_{0.25}Lu_{0.25}Yb_{0.25}Eu_{0.25})_2SiO_5$ (125.4±8.7 μm) is smaller than those of Eu_2SiO_5, Ho_2SiO_5, and the average of the four RE_2SiO_5 (132.6±10.7 μm), suggesting good CMAS resistance. The CMAS attacks RE_2SiO_5 through the dissolution of RE_2SiO_5 into CMAS with the precipitation of $Ca_2RE_8(SiO_4)_6O_2$. Dissolution and precipitation will proceed until the residual CMAS reaches equilibrium. $(Ho_{0.25}Lu_{0.25}Yb_{0.25}Eu_{0.25})_2SiO_5$ incorporates Ho, Lu, Yb, and Eu elements. The formation enthalpy of $Ca_2RE_8(SiO_4)_6O_2$ (RE = Ho, Lu, Yb, and Eu) are different [50]. Hence, Lu, Yb, Ho, and Eu ions present a gradient velocity in the precipitation of $Ca_2RE_8(SiO_4)_6O_2$ [51]. Yb and Lu with small ionic radii will slow down the formation of reaction product $Ca_2RE_8(SiO_4)_6O_2$ which is comprised of Lu, Yb, Ho, and Eu elements (Table 7). Our previous work has revealed that the resistance to CMAS corrosion of RE_2SiO_5 (RE = Tb, Dy, Ho, Er, Y, Tm, Yb, and Lu) at 1300 ℃ increases with the reduction of the radius of RE^{3+} [12]. Consequently, Lu and Yb in $(Ho_{0.25}Lu_{0.25}Yb_{0.25}Eu_{0.25})_2SiO_5$ effectively mitigate CMAS corrosion.

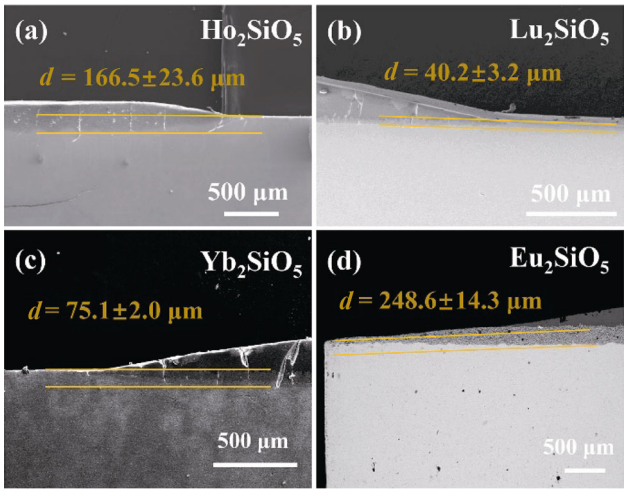

Fig. 14 Cross-sectional morphologies of (a) Ho_2SiO_5, (b) Lu_2SiO_5, (c) Yb_2SiO_5, and (d) Eu_2SiO_5 after CMAS corrosion at 1300 ℃ for 20 h.

The thermal conductivity, thermal expansion coefficient, reduced modulus, and CMAS corrosion resistance of $(Ho_{0.25}Lu_{0.25}Yb_{0.25}Eu_{0.25})_2SiO_5$ were compared with the average value of Ho_2SiO_5, Lu_2SiO_5, Yb_2SiO_5, and Eu_2SiO_5, as shown in Fig. 15. The high-entropy $(Ho_{0.25}Lu_{0.25}Yb_{0.25}Eu_{0.25})_2SiO_5$ ceramic exhibits excellent thermal insulation properties, tunable TEC, low reduced modulus, and good resistance to CMAS corrosion. The above results demonstrate that $(Ho_{0.25}Lu_{0.25}Yb_{0.25}Eu_{0.25})_2SiO_5$ is a promising EBC candidate.

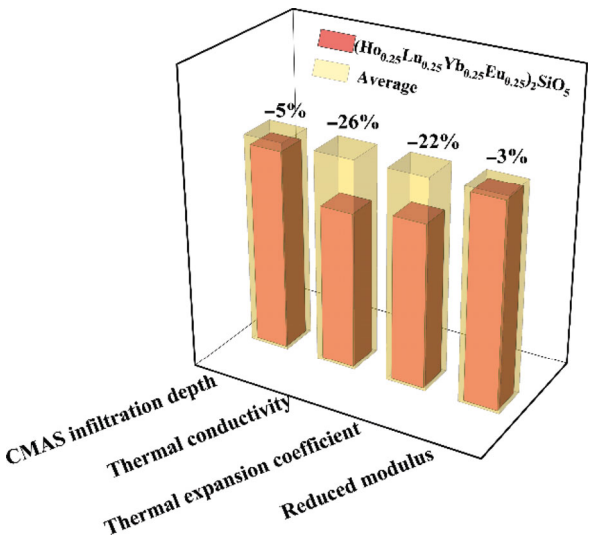

Fig. 15 Comparison of thermal conductivity, thermal expansion coefficient, reduced modulus, and CMAS infiltration depth of $(Ho_{0.25}Lu_{0.25}Yb_{0.25}Eu_{0.25})_2SiO_5$ with the average values of Ho_2SiO_5, Lu_2SiO_5, Yb_2SiO_5, and Eu_2SiO_5.

4 Conclusions

In this study, a novel high-entropy RE silicate ceramic $(Ho_{0.25}Lu_{0.25}Yb_{0.25}Eu_{0.25})_2SiO_5$ was designed and successfully fabricated. $(Ho_{0.25}Lu_{0.25}Yb_{0.25}Eu_{0.25})_2SiO_5$ shows very low thermal conductivity, exhibiting excellent thermal insulation properties. Oxygen vacancies and severe lattice distortion mainly contribute to the low thermal conductivity. The TEC of $(Ho_{0.25}Lu_{0.25}Yb_{0.25}Eu_{0.25})_2SiO_5$ from room temperature to 1200 ℃ is $(4.0 - 5.9) \times 10^{-6}$ K^{-1}, which is close to that of SiC. The reduced modulus of $(Ho_{0.25}Lu_{0.25}Yb_{0.25}Eu_{0.25})_2SiO_5$ is 149.0± 16.5 GPa which is lower than those of Lu_2SiO_5, Yb_2SiO_5, and the average of RE_2SiO_5 (RE = Ho, Lu, Yb, and Eu). In addition, $(Ho_{0.25}Lu_{0.25}Yb_{0.25}Eu_{0.25})_2SiO_5$ presents good CMAS corrosion resistance. $Ca_2RE_8(SiO_4)_6O_2$ and garnet-type phase $(Ca_xRE_{3-x})(Mg_yAl_zSi_{5-y-z})O_{12}$ are the main reaction products. Excellent thermal insulation properties, suitable TEC, low reduced modulus, and good CMAS corrosion resistance of $(Ho_{0.25}Lu_{0.25}Yb_{0.25}Eu_{0.25})_2SiO_5$ make it a potential EBC material candidate.

Acknowledgements

This work was financially supported by Guangdong Basic and Applied Basic Research Foundation for Distinguished Young Scholars (Grant No. 2021B1515020083), Guang Dong Basic and Applied Basic Research Foundation for Young Scholars (Grant No. 21201910240002803), Shenzhen Science and Technology Program (Grant Nos. GXWD20201231165807008, 20200831172254001), and Fundamental Research Funds for the Central Universities, Sun Yat-sen University (Grant No. 2021qntd10). The authors are grateful to Dr. Wenxia Zhao from Sun Yat-sen University Instrumental Analysis & Research Center for her kind help with EPMA analysis.

Declaration of competing interest

The authors have no competing interests to declare that are relevant to the content of this article.

References

[1] Padture NP, Gell M, Jordan EH. Thermal barrier coatings for gas-turbine engine applications. *Science* 2002, **296**: 280–284.

[2] Richards BT, Wadley HNG. Plasma spray deposition of

tri-layer environmental barrier coatings. *J Eur Ceram Soc* 2014, **34**: 3069–3083.

[3] Lee KN. Key durability issues with mullite-based environmental barrier coatings for Si-based ceramics. *J Eng Gas Turbines Power* 2000, **122**: 632–636.

[4] Jacobson NS, Smialek JL, Fox DS. Molten salt corrosion of SiC and Si_3N_4. In: *Handbook of Ceramics and Composites*. Boca Raton: CRC Press, 1990: 99–135.

[5] Padture NP. Environmental degradation of high-temperature protective coatings for ceramic-matrix composites in gas-turbine engines. *npj Mater Degrad* 2019, **3**: 11.

[6] Tejero-Martin D, Bennett C, Hussain T. A review on environmental barrier coatings: History, current state of the art and future developments. *J Eur Ceram Soc* 2021, **41**: 1747–1768.

[7] Harada Y, Suzuki T, Hirano K, *et al*. Environmental effects on ultra-high temperature creep behavior of directionally solidified oxide eutectic ceramics. *J Eur Ceram Soc* 2005, **25**: 1275–1283.

[8] Kitamura J, Tang ZL, Mizuno H, *et al*. Structural, mechanical and erosion properties of yttrium oxide coatings by axial suspension plasma spraying for electronics applications. *J Therm Spray Technol* 2011, **20**: 170–185.

[9] Liu J, Zhang LT, Liu QM, *et al*. Calcium–magnesium–aluminosilicate corrosion behaviors of rare-earth disilicates at 1400 ℃. *J Eur Ceram Soc* 2013, **33**: 3419–3428.

[10] Harder BJ, Ramìrez-Rico J, Almer JD, *et al*. Chemical and mechanical consequences of environmental barrier coating exposure to calcium–magnesium–aluminosilicate. *J Am Ceram Soc* 2011, **94**: 178–185.

[11] Bakan E, Sohn YJ, Kunz W, *et al*. Effect of processing on high-velocity water vapor recession behavior of Yb–silicate environmental barrier coatings. *J Eur Ceram Soc* 2019, **39**: 1507–1513.

[12] Tian ZL, Zhang J, Zheng LY, *et al*. General trend on the phase stability and corrosion resistance of rare earth monosilicates to molten calcium–magnesium–aluminosilicate at 1300 ℃. *Corros Sci* 2019, **148**: 281–292.

[13] Ueno S, Ohji T, Lin HT. Recession behavior of a silicon nitride with multi-layered environmental barrier coating system. *Ceram Int* 2007, **33**: 859–862.

[14] Richards BT, Young KA, de Francqueville F, *et al*. Response of ytterbium disilicate-silicon environmental barrier coatings to thermal cycling in water vapor. *Acta Mater* 2016, **106**: 1–14.

[15] Tian ZL, Zheng LY, Wang JM, *et al*. Theoretical and experimental determination of the major thermo-mechanical properties of RE_2SiO_5 (RE = Tb, Dy, Ho, Er, Tm, Yb, Lu, and Y) for environmental and thermal barrier coating applications. *J Eur Ceram Soc* 2016, **36**: 189–202.

[16] Liu D, Liu HH, Ning SS, *et al*. Chrysanthemum-like high-entropy diboride nanoflowers: A new class of high-entropy nanomaterials. *J Adv Ceram* 2020, **9**: 339–348.

[17] Zhao ZF, Chen H, Xiang HM, *et al*. High entropy defective fluorite structured rare-earth niobates and tantalates for thermal barrier applications. *J Adv Ceram* 2020, **9**: 303–311.

[18] Zheng YP, Zou MC, Zhang WY, *et al*. Electrical and thermal transport behaviours of high-entropy perovskite thermoelectric oxides. *J Adv Ceram* 2021, **10**: 377–384.

[19] Zhao ZF, Xiang HM, Chen H, *et al*. High-entropy $(Nd_{0.2}Sm_{0.2}Eu_{0.2}Y_{0.2}Yb_{0.2})_4Al_2O_9$ with good high temperature stability, low thermal conductivity, and anisotropic thermal expansivity. *J Adv Ceram* 2020, **9**: 595–605.

[20] Qin MD, Yan QZ, Liu Y, *et al*. A new class of high-entropy M_3B_4 borides. *J Adv Ceram* 2021, **10**: 166–172.

[21] Sun YN, Xiang HM, Dai FZ, *et al*. Preparation and properties of CMAS resistant bixbyite structured high-entropy oxides RE_2O_3 (RE = Sm, Eu, Er, Lu, Y, and Yb): Promising environmental barrier coating materials for Al_2O_{3f}/Al_2O_3 composites. *J Adv Ceram* 2021, **10**: 596–613.

[22] Xiang HM, Xing Y, Dai FZ, *et al*. High-entropy ceramics: Present status, challenges, and a look forward. *J Adv Ceram* 2021, **10**: 385–441.

[23] Ren XM, Tian ZL, Zhang J, *et al*. Equiatomic quaternary $(Y_{1/4}Ho_{1/4}Er_{1/4}Yb_{1/4})_2SiO_5$ silicate: A perspective multifunctional thermal and environmental barrier coating material. *Scripta Mater* 2019, **168**: 47–50.

[24] Liao W, Tan YQ, Zhu CW, *et al*. Synthesis, microstructures, and corrosion behaviors of multi-components rare-earth silicates. *Ceram Int* 2021, **47**: 32641–32647.

[25] Tian ZL, Zhang J, Zhang TY, *et al*. Towards thermal barrier coating application for rare earth silicates RE_2SiO_5 (RE = La, Nd, Sm, Eu, and Gd). *J Eur Ceram Soc* 2019, **39**: 1463–1476.

[26] Toby BH. EXPGUI, a graphical user interface for GSAS. *J Appl Cryst* 2001, **34**: 210–213.

[27] Roufosse M, Klemens PG. Thermal conductivity of complex dielectric crystals. *Phys Rev B* 1973, **7**: 5379–5386.

[28] Leitner J, Chuchvalec P, Sedmidubský D, *et al*. Estimation of heat capacities of solid mixed oxides. *Thermochimica Acta* 2002, **395**: 27–46.

[29] Charvat FR, Kingery WD. Thermal conductivity: XIII, effect of microstructure on conductivity of single-phase ceramics. *J Am Ceram Soc* 1957, **40**: 306–315.

[30] Clarke DR. Materials selection guidelines for low thermal conductivity thermal barrier coatings. *Surf Coat Technol* 2003, **163–164**: 67–74.

[31] Levi CG, Hutchinson JW, Vidal-Sétif MH, *et al*. Environmental degradation of thermal-barrier coatings by molten deposits. *MRS Bull* 2012, **37**: 932–941.

[32] Wang JG, Tian SJ, Li GB, *et al*. Preparation and X-ray characterization of low-temperature phases of R_2SiO_5 (R = rare earth elements). *Mater Res Bull* 2001, **36**: 1855–1861.

[33] Tian ZL, Sun LC, Wang JM, *et al*. Theoretical prediction and experimental determination of the low lattice thermal conductivity of Lu_2SiO_5. *J Eur Ceram Soc* 2015, **35**: 1923–1932.

[34] Berman R. The thermal conductivities of some dielectric solids at low temperatures (experimental). *Proc R Soc Lond A* 1951, **208**: 90–108.

[35] Bruls RJ, Hintzen HT, Metselaar R. A new estimation method for the intrinsic thermal conductivity of nonmetallic compounds: A case study for $MgSiN_2$, AlN and β-Si_3N_4 ceramics. *J Eur Ceram Soc* 2005, **25**: 767–779.

[36] Klemens PG. Thermal resistance due to point defects at high temperatures. *Phys Rev* 1960, **119**: 507–509.

[37] Tian ZL, Lin CF, Zheng LY, *et al*. Defect-mediated multiple-enhancement of phonon scattering and decrement of thermal conductivity in $(Y_xYb_{1-x})_2SiO_5$ solid solution. *Acta Mater* 2018, **144**: 292–304.

[38] Wan CL, Pan W, Xu Q, *et al*. Effect of point defects on the thermal transport properties of $(La_xGd_{1-x})_2Zr_2O_7$: Experiment and theoretical model. *Phys Rev B* 2006, **74**: 144109.

[39] Zhao M, Pan W, Li TJ, *et al*. Oxygen-vacancy-mediated microstructure and thermophysical properties in $Zr_3Ln_4O_{12}$ for high-temperature applications. *J Am Ceram Soc* 2019, **102**: 1961–1970.

[40] Matsudaira T, Wada M, Kawashima N, *et al*. Mass transfer in polycrystalline ytterbium monosilicate under oxygen potential gradients at high temperatures. *J Eur Ceram Soc* 2021, **41**: 3150–3160.

[41] Grant KM, Krämer S, Löfvander JPA, *et al*. CMAS degradation of environmental barrier coatings. *Surf Coat Technol* 2007, **202**: 653–657.

[42] Nasiri NA, Patra N, Horlait D, *et al*. Thermal properties of rare-earth monosilicates for EBC on Si-based ceramic composites. *J Am Ceram Soc* 2016, **99**: 589–596.

[43] Li YR, Luo YX, Tian ZL, *et al*. Theoretical exploration of the abnormal trend in lattice thermal conductivity for monosilicates RE_2SiO_5 (RE = Dy, Ho, Er, Tm, Yb and Lu). *J Eur Ceram Soc* 2018, **38**: 3539–3546.

[44] Cong HJ, Zhang HJ, Wang JY, *et al*. Structural and thermal properties of the monoclinic Lu_2SiO_5 single crystal: Evaluation as a new laser matrix. *J Appl Cryst* 2009, **42**: 284–294.

[45] Gao LY, Luo YX, Wan P, *et al*. Theoretical and experimental investigations on mechanical properties of $(Fe,Ni)Sn_2$ intermetallic compounds formed in SnAgCu/Fe–Ni solder joints. *Mater Charact* 2021, **178**: 111195.

[46] Menke Y, Peltier-Baron V, Hampshire S. Effect of rare-earth cations on properties of sialon glasses. *J Non Cryst Solids* 2000, **276**: 145–150.

[47] Pan ZF, Chen JC, Wu HQ, *et al*. Red emission enhancement in Ce^{3+}/Mn^{2+} co-doping suited garnet host $MgY_2Al_4SiO_{12}$ for tunable warm white LED. *Opt Mater* 2017, **72**: 257–264.

[48] Miara LJ, Ong SP, Mo YF, *et al*. Effect of Rb and Ta doping on the ionic conductivity and stability of the garnet $Li_{7+2x-y}(La_{3-x}Rb_x)(Zr_{2-y}Ta_y)O_{12}$ ($0 \leqslant x \leqslant 0.375$, $0 \leqslant y \leqslant 1$) superionic conductor: A first principles investigation. *Chem Mater* 2013, **25**: 3048–3055.

[49] Arsad AZ, Ibrahim NB. The effect of Ce doping on the structure, surface morphology and magnetic properties of Dy doped-yttrium iron garnet films prepared by a sol-gel method. *J Magn Magn Mater* 2016, **410**: 128–136.

[50] Costa G, Harder BJ, Bansal NP, *et al*. Thermochemistry of calcium rare-earth silicate oxyapatites. *J Am Ceram Soc* 2020, **103**: 1446–1453.

[51] Tu TZ, Liu JX, Zhou L, *et al*. Graceful behavior during CMAS corrosion of a high-entropy rare-earth zirconate for thermal barrier coating material. *J Eur Ceram Soc* 2022, **42**: 649–657.